



# Methylene blue photodegradation over titania-decorated SBA-15

Y.J. Acosta-Silva<sup>a</sup>, R. Nava<sup>a,\*</sup>, V. Hernández-Morales<sup>a</sup>, S.A. Macías-Sánchez<sup>a</sup>,  
M.L. Gómez-Herrera<sup>a</sup>, B. Pawelec<sup>b</sup>

<sup>a</sup> División de Investigación y Posgrado, Facultad de Ingeniería, Universidad Autónoma de Querétaro (UAQ), Centro Universitario, 76000 Querétaro, Qro., Mexico

<sup>b</sup> Instituto de Catálisis y Petroleoquímica, CSIC, Cantoblanco, 28049 Madrid, Spain

## ARTICLE INFO

### Article history:

Received 1 May 2011

Received in revised form 28 June 2011

Accepted 25 August 2011

Available online 1 September 2011

### Keywords:

Photocatalysis

Methylene blue

Mesoporous matrices

Titania

SBA-15

## ABSTRACT

Santa Barbara Amorphous (SBA-15) mesoporous materials decorated with vary amount of TiO<sub>2</sub> (7–31% TiO<sub>2</sub>/SBA-15) were prepared by the post-synthesis method from previously synthesized SBA-15 and their photocatalytic activity toward the degradation of methylene blue (MB) was measured. Nonionic surfactant was used as liquid template and tetraethyl orthosilicate (TEOS) as SiO<sub>2</sub> precursor for the synthesis of mesoporous silica SBA-15. The synthesized x% TiO<sub>2</sub>/SBA-15 materials were characterized by N<sub>2</sub> adsorption–desorption isotherms, X-ray diffraction (XRD), UV–vis diffuse reflectance spectroscopy (UV–vis DRS), micro-Raman spectroscopy, infrared spectroscopy of framework vibration (IR-KBr) and X-ray photoelectron spectroscopy (XPS). The x% TiO<sub>2</sub>/SBA-15 photocatalysts were found to be more active than pure anatase titania and this increase was linear with TiO<sub>2</sub> loading. The highest activity of 31% TiO<sub>2</sub>/SBA-15 sample was explained in terms of the combined factors such as a high crystallinity of anatase phase, preservation of a high surface area, a large amount of the surface hydroxyl groups, and a larger accessibility of photo-oxidative sites. A linear correlation between the apparent first order rate constants ( $k_{app}$ ) and the amount of TiO<sub>2</sub> species located within porous structure of the SBA-15 substrate was found.

© 2011 Elsevier B.V. All rights reserved.

## 1. Introduction

Dyes are extensively used, especially in the textile, leather, pulp and paper, and cosmetic industries, and the discharge of effluents from these applications is a major contributor of color in water sources [1–3]; in particular, textile industries are responsible for the discharge of the largest amount of colored effluents in water. The estimated annual production of commercially available dyes is approximately  $7 \times 10^5$  tons, which includes more than 100,000 dyes. Methylene blue (C<sub>16</sub>H<sub>18</sub>N<sub>3</sub>SCl·3H<sub>2</sub>O) is one of the most applied dyes [4], it is an important basic dye widely used for printing calico, cotton and tannin, indicating oxidation–reduction, and dyeing leather. In purified zinc-free form, it is used as an anti-septic and for other medicinal purposes [5]. Dyes are generally non-degradable and constitute a problematic group of pollutants. Dyes are harmful to flora and fauna, and some of the dyes have been reported to be carcinogenic and mutagenic [6].

Photocatalysis on semiconductor surfaces using TiO<sub>2</sub> is of current interest especially in order to tackle a variety of environmental problems like waste-water treatment and remediation, hazardous

waste control, water disinfection and air purification. The TiO<sub>2</sub> is biologically and chemically inert, nontoxic, inexpensive and is resistant to both photocorrosion and chemical corrosion [7,8]. Using ultra-violet light, electron–hole pairs can be generated in the TiO<sub>2</sub> semiconductor particles as long as the UV photon energies are greater than the TiO<sub>2</sub> bandgap energy (3.2 eV) [9,10]. The generated holes are a strong oxidizing agent ( $E = +2.8$  V). The reaction of the photogenerated holes with water molecules and hydroxyl ions adsorbed on the surface of TiO<sub>2</sub> yields formation of hydroxyl radicals (\*OH), capable of mineralizing organic compounds to carbon dioxide and water [11].

The fine powders of titania exhibit high photocatalytic activity since the accessibility of these small surfaces for organic pollutants is high. For industrial applications however, several problems occur. The small particles are difficult to recover by filtration or centrifugation after the reaction [12,13]. Moreover in aqueous applications, the particles will agglomerate resulting in a decreased photocatalytic activity [14].

To maximize the photocatalytic activity of TiO<sub>2</sub>, particles should be small enough to offer high specific surface areas since it is important for a heterogeneous photocatalyst to have such an area with a high number of reactive sites. Therefore, researchers often use TiO<sub>2</sub> with small particle sizes, leading to a high surface area and photocatalytic activity [15]. These problems have motivated the development of supported photocatalysts in which TiO<sub>2</sub> has been

\* Corresponding author. Tel.: +52 442 192 12 00x6016;

fax: +52 442 192 12 00x6006.

E-mail address: [rufino@uaq.mx](mailto:rufino@uaq.mx) (R. Nava).

immobilized on diverse materials. This increases the surface area without decreasing the particle size in order to easily separate and reuse the photocatalyst [16]. After the discovery of MCM materials [17], much research has been done to synthesize all kinds of mesoporous siliceous materials. The efforts made on the synthesis of these systems resulted in a wide range of pore structures, pore diameters, stabilities and adsorption capacities.

The SBA-15, synthesized by Zhao et al. [18,19], is one of the most intensively studied mesoporous silica material due to its easy synthesis and good thermal and hydrothermal stability. SBA-15 has large tailorable uniform pores (3–15 nm), thick amorphous silica walls (3–6 nm) and high surface areas (700–800 m<sup>2</sup>/g). One way to combine mesoporous silica with titania active centers is to synthesize the siliceous support material and subsequently deposit titania on the surface by applying post-synthesis methods [20–24]. Here, the SiO<sub>2</sub> support material is first prepared and then loaded with TiO<sub>2</sub>. Commercial SiO<sub>2</sub> [25,26], zeolite [27], clays [28–30], SiO<sub>2</sub> spheres [31,32] and ordered SiO<sub>2</sub> materials, like MCM-41 [33] have already been activated with TiO<sub>2</sub>. The TiO<sub>2</sub> loading can be varied ranging from 3 to 80 wt.% [25,27,33]. Different post-modification methods have been described in literature to deposit crystalline TiO<sub>2</sub> on different supports: acid-catalysed sol–gel method [26,27], chemical solution deposition [34], internal hydrolysis [34] or multistep deposition [22,35,36]. Introducing titanium species into mesoporous silicate materials has attracted much interest because the titanium-containing mesoporous systems have much higher active surface areas (>200 m<sup>2</sup>/g) in comparison to pure titania [37], which makes them more effective.

Linking chemically TiO<sub>2</sub> particles and dispersing them inside the pores of mesoporous SBA-15 materials allows with a suitable mean pore size induce controlled oxide particle growth, uniformity of size, as well as to stabilize and prevent agglomeration of the particles. Thus, this approach generates a large number of active sites which are used for adsorption/desorption of reactants or products.

Within this scenario, in the present work we report the *ex situ* synthesis of the mesoporous matrices x% TiO<sub>2</sub>/SBA-15 with variable quantity of TiO<sub>2</sub> and its effect on the photodegradation of methylene blue. The photodegradation activity of the photocatalysts was evaluated in a liquid-phase reactor using UV–vis spectroscopy to monitor the change of the dye concentration. Furthermore, the structural characterization of the mesoporous matrices has been performed using several techniques such as N<sub>2</sub> adsorption–desorption isotherms, X-ray diffraction (XRD), infrared spectroscopy of framework vibration (IR-KBr), Micro-Raman spectroscopy, UV–vis diffuse reflectance spectroscopy (UV–vis DRS) and X-ray photoelectron spectroscopy (XPS).

## 2. Experimental

### 2.1. Preparation of the SBA-15 support

Siliceous SBA-15 mesoporous material was synthesized according to the procedure described by Flodström and Alfredsson [38]. The Pluronic triblock copolymer (BASF, EO<sub>20</sub>–PO<sub>70</sub>–EO<sub>20</sub>, P123) was used as the structure-directing agent and tetraethylorthosilicate (TEOS, 98%, Aldrich) as a source of silica. In a typical synthesis, the triblock copolymer was dissolved in a mixture of deionized water and 4 M hydrochloric acid solution stirred for 1 h, after which the required amount of TEOS was added to the solution at 308 K and kept under stirring conditions for 24 h. The mixture was subsequently transferred into polypropylene bottles and heated at 353 K for 24 h. After synthesis, the obtained solid was filtered, washed thoroughly with distilled water, dried at 383 K for 18 h and finally was calcined at 823 K for 4 h to remove the organic template [39].

### 2.2. Modification of mesoporous SBA-15 with TiO<sub>2</sub> particles

The decoration of SBA-15 with TiO<sub>2</sub> clusters was realized according to the procedure described by Peza-Ledesma et al. [39]. The titania-containing SBA-15 mesoporous systems were synthesized using as source of TiO<sub>2</sub>, titanium(IV) isopropoxide (97%, Aldrich, IPOTi) in 2-propanol (99.5% Sigma–Aldrich). The modification of SBA-15 was performed by the post-synthesis method (*ex situ*) from the previously synthesized SBA-15. Mesoporous silica was dispersed in a solution of IPOTi (precursor of TiO<sub>2</sub> particles) and 2-propanol. The concentration of IPOTi was calculated to obtain 1.5 g of SBA-15 modified with different percentages of TiO<sub>2</sub> (7–31 wt.%). The TiO<sub>2</sub> particles were formed at room temperature in an inert atmosphere of N<sub>2</sub> for 1 h. Then, deionized water was slowly added and the liquid suspension was stirred for 30 min. Finally, the solids were dried at room temperature and later at 383 K for 18 h before being calcined at 823 K for 4 h [39].

### 2.3. Characterization methods

#### 2.3.1. Chemical analysis

The TiO<sub>2</sub> loadings of the TiO<sub>2</sub>/SBA-15 matrices were determined by inductively coupled plasma atomic emission spectroscopy (ICP–AES), Perkin Elmer Optima 3300DV. The solid samples were first digested (in a mixture of HF, HCl and HNO<sub>3</sub>) in a microwave oven for 2 h. Then, aliquots of solution were diluted to 50 mL using deionized water (18.2 mΩ quality).

#### 2.3.2. N<sub>2</sub> adsorption–desorption isotherms

The textural properties of the mesoporous matrices were determined from the nitrogen adsorption isotherms recorded at 77 K with a Micromeritics TriStar 3000 apparatus. The samples were previously degassed at 423 K for 24 h under a vacuum (10<sup>−4</sup> mbar) to ensure a clean, dry surface, free of any loosely bound adsorbed species. The specific areas of the samples were calculated according to standard BET procedure using nitrogen adsorption data collected in the relative equilibrium pressure interval of 0.03 < P/P<sub>0</sub> < 0.3. Pore size distributions were calculated from the desorption branches of the corresponding nitrogen isotherm using the BJH method. The total pore volume (V<sub>total</sub>) was estimated from the amount of nitrogen adsorbed at a relative pressure of 0.99.

#### 2.3.3. X-ray diffraction (XRD)

XRD measurements of the samples in powder were carried out using the Cu Kα radiation with a wavelength of 1.54 Å in two ranges: 0.5–3° (low-angle) and 10–80° (wide-angle) on a Rigaku model MAXD diffractometer. Particle size calculation was made using the Scherrer equation.

#### 2.3.4. Infrared spectroscopy of framework vibration

Fourier transform-IR (FT-IR) spectra of the mesoporous matrices TiO<sub>2</sub>/SBA-15 were recorded by means of a Bruker Vector 3.3 spectrophotometer using the KBr wafer technique in 400–1800 cm<sup>−1</sup> range.

#### 2.3.5. Micro-Raman spectroscopy

Raman spectroscopy (RS) was carried out using a Labram–Dior Raman model microspectrometer, with a He–Ne laser that emitted a wavelength of 632.8 nm and a power of 15 mW. The Raman spectra samples were measured at room temperature in a wavelength range between 50 and 1100 nm, using a 50× objective to focalize the laser spot.

#### 2.3.6. Diffuse reflectance spectroscopy (DRS)

The UV–vis diffuse reflectance spectra of the mesoporous matrices were recorded at room temperature using an Ocean Optics Inc.

spectrometer First in Photonics (Mini-DT 2) in the 200–400 nm range. The respective support of each mesoporous matrix was used as a reference.

### 2.3.7. X-ray photoelectron spectroscopy (XPS)

The state of Ti in the mesoporous TiO<sub>2</sub>/SBA-15 matrices was determined by the XPS technique using VG Escalab 200R electron spectrometer equipped with a hemispherical electron analyzer, using a Mg K $\alpha$  ( $h\nu = 1253.6$  eV,  $1 \text{ eV} = 1.603 \times 10^{-19}$  J) X-ray source. After outgassing at  $10^{-6}$  mbar, the samples were transferred to the ion-pumped analysis chamber, in which the residual pressure was kept below  $4 \times 10^{-9}$  mbar during data acquisition. The binding energy (BE) of the C 1s peak at 284.8 eV was taken as an internal standard. The accuracy of the BE values was  $\pm 0.1$  eV. Peak intensities were estimated by calculating the integral of each peak after subtracting an S-shaped background and fitting the experimental peak to a combination of Lorentzian/Gaussian lines of variable proportions. Ti/Si atomic ratio was estimated from the areas of the peaks corrected using the corresponding sensitivity factors [40].

### 2.4. Photocatalytic activity

The photodegradation of methylene blue (99%, Aldrich, MB) was performed in order to evaluate the photocatalytic activity of prepared titania/silica systems. The experiments were carried out in a cylindrical double wall jacket glass reactor containing 100 mL of MB solution with an initial concentration of 40 mg/L. The mixture was first stirred for 15 min in the dark at room temperature to assure that the adsorption equilibrium was reached. Then the reaction solution was placed perpendicularly to a 125 W medium pressure mercury lamp inside cold water and the solution was bubbled with air under magnetic agitation. Commercial pure TiO<sub>2</sub> (P-25, Degussa Co., Germany) of 30.0 mg was used as reference photocatalyst. The amount of x% TiO<sub>2</sub>/SiO<sub>2</sub> catalyst used in each experiment was adjusted to achieve the same TiO<sub>2</sub> loading as those of reference sample. The comparison of tested catalysts was done at this fixed TiO<sub>2</sub> concentration because in our experimental conditions, only the semiconductor particles were expected to show photocatalytic activity. Suspension samples of 5 mL volume were collected at fixed time intervals, following centrifugation and the concentration of MB was determined by UV–vis spectroscopy (Varian Cary 5000 Scan UV–vis–NIR spectrophotometer). The photocatalytic degradation of methylene blue of irradiated and non-irradiated (in dark) samples were determined by means of UV–vis spectrophotometry through monitoring of color disappearance. A calibration curve of MB solution absorbent was obtained at 665 nm wavelength at different concentrations prepared. The concentration of MB at different irradiation times was obtained by converting absorbance of the solution to MB concentration (Beer–Lambert's law,  $A = \epsilon bC$ , where  $A$ : absorption,  $\epsilon$ : proportion constant,  $b$ : light length,  $C$ : concentration). A standard calibration curve (not shown here) was built by adjusting a different concentration of MB solution and the absorption at 665 nm. This calibration curve refers to the situation of the absence of by-products co-adsorption. A blank test was done in the solution without a catalyst, where the concentration of the MB indicates constancy. Unfortunately, there is no way to evaluate the extent of mineralization the MB into harmless gaseous CO<sub>2</sub>, NH<sub>4</sub><sup>+</sup> and NO<sub>3</sub><sup>−</sup> using UV/vis technique employed.

## 3. Results and discussion

### 3.1. Chemical and textural properties

In the present work, SBA-15 mesoporous material was decorated with different amount of TiO<sub>2</sub>. The quantification of TiO<sub>2</sub>

**Table 1**

Chemical<sup>a</sup> and textural<sup>b</sup> properties of SBA-15 and TiO<sub>2</sub>/SBA-15 mesoporous materials.

Sample	TiO <sub>2</sub> (wt.%)	$S_{\text{BET}}$ (m <sup>2</sup> /g)	$NS_{\text{BET}}$	$V_{\text{total}}$ (m <sup>3</sup> /g)	$d$ (nm)
SBA-15	0.0	932	–	1.05	5.9
7% TiO <sub>2</sub> /SBA-15	7.3	659	0.76	0.83	5.0
12% TiO <sub>2</sub> /SBA-15	12.0	505	0.62	0.69	5.0
18% TiO <sub>2</sub> /SBA-15	17.5	507	0.66	0.52	4.1
22% TiO <sub>2</sub> /SBA-15	21.9	544	0.75	0.58	4.7
26% TiO <sub>2</sub> /SBA-15	26.2	476	0.69	0.56	4.9
31% TiO <sub>2</sub> /SBA-15	31.1	395	0.62	0.34	3.5

<sup>a</sup> As determined by ICP technique.

<sup>b</sup> Specific BET surface area ( $S_{\text{BET}}$ ), total pore volume ( $V_{\text{pore}}$ ) and pore diameter ( $d$ ) as determined by N<sub>2</sub> physisorption at 196 °C.  $NS_{\text{BET}}$ : normalized  $S_{\text{BET}}$  calculated from equation  $NS_{\text{BET}} = (S_{\text{BET}} \text{ of } x\% \text{ TiO}_2/\text{SBA-15}) / [(1 - y) \times S_{\text{BET}} \text{ of naked SBA-15}]$ , where  $y$  is the TiO<sub>2</sub> loading determined by ICP-AES.

present in the synthesized x% TiO<sub>2</sub>/SBA-15 samples (from chemical analysis) is presented in Table 1. As seen in this table, the TiO<sub>2</sub> content of all hybrid materials fall in the range 7.3–31.1 wt.%. The textural properties of the mesoporous matrices were studied by N<sub>2</sub> adsorption–desorption isotherms at 77 K. The N<sub>2</sub> adsorption–desorption isotherms of the materials are presented in Fig. 1. All x% TiO<sub>2</sub>/SBA-15 mesoporous samples as well as the pure SBA-15 exhibit adsorption isotherms type IV with H1 hysteresis loops according to IUPAC classification [41]. These isotherms are characteristic of mesoporous materials with a hexagonal arrangement of pores [42,43]. As seen in Fig. 1, the N<sub>2</sub> adsorption–desorption isotherms of the mesoporous matrices x% TiO<sub>2</sub>/SBA-15 are similar, indicating that the mesostructure of the SBA-15 material was maintained upon TiO<sub>2</sub> incorporation. The SBA-15 sample presents the hysteresis loop in a range well defined at high relative pressures ( $0.61 < P/P_0 < 0.8$ ) that represents the spontaneous filling of the mesopores due to capillary condensation, indicating the presence of uniform mesopores. The modified meso-

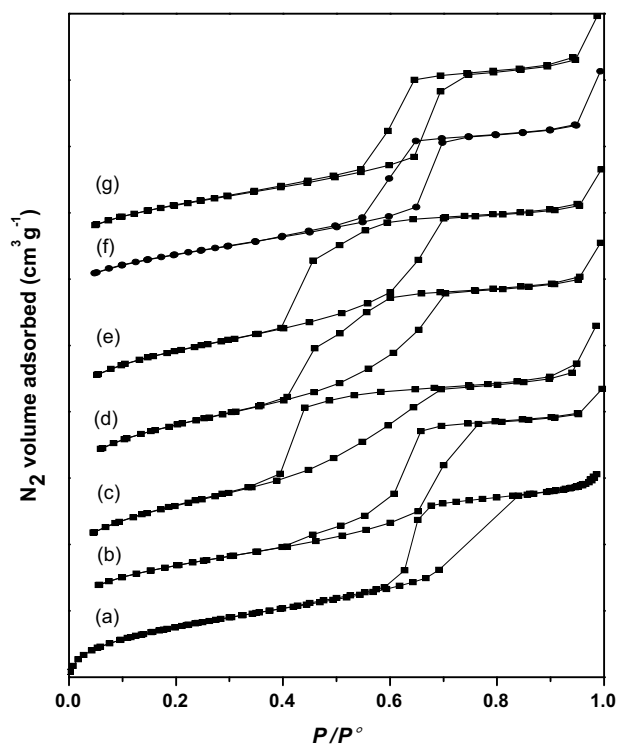


**Fig. 1.** N<sub>2</sub> adsorption–desorption isotherms of x% TiO<sub>2</sub>/SBA-15 mesoporous samples: (a), naked SBA-15; (b), 7% TiO<sub>2</sub>; (c), 12% TiO<sub>2</sub>; (d), 18% TiO<sub>2</sub>; (e), 22% TiO<sub>2</sub>; (f), 26% TiO<sub>2</sub>; and (g), 31% TiO<sub>2</sub>.

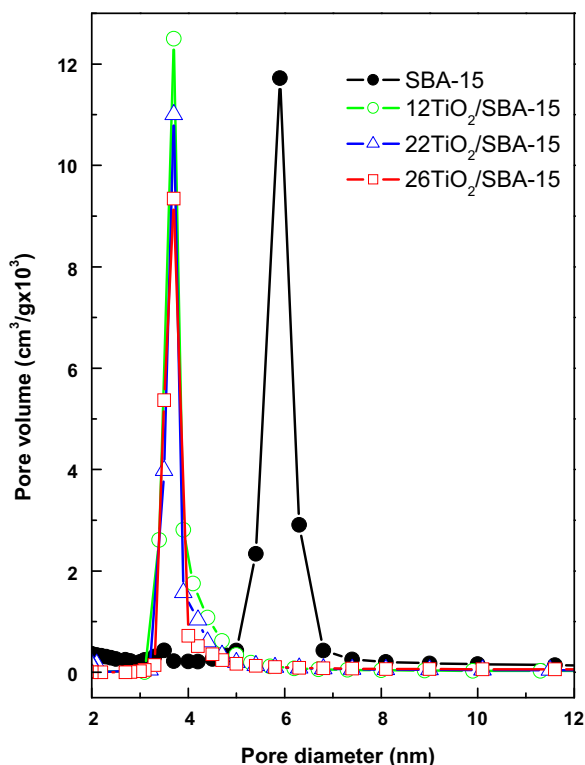


**Fig. 2.** Pore size distribution of the  $x\%$  TiO<sub>2</sub>/SBA-15 and SBA-15 samples calculated from the adsorption branch of the N<sub>2</sub> isotherm using the by BJH method.

porous TiO<sub>2</sub> matrices show hysteresis loops at intervals of lower relative pressures ( $0.4 < P/P_0 < 0.7$ ) due to a decrease in the size of the mesopores by the presence of small TiO<sub>2</sub> particles dispersed within the pores of SBA-15.

Concerning the pore size distribution shown in Fig. 2, it should be noted that all mesoporous matrices show a uniform, narrow pore size distribution. There appears to be a pore diameter shift to smaller diameter upon an increase of TiO<sub>2</sub> loading. Simultaneously, the total N<sub>2</sub> volume ( $V_{\text{total}}$ ) decreased with increasing TiO<sub>2</sub> loading in the mesoporous matrices (Table 1). As expected, titania loading on the silica matrix decreases surface area and pore volume of the SBA-15 support (Table 1). Besides this, the BET area values of all  $x\%$  TiO<sub>2</sub>/SBA-15 materials are very high (in range 659–395 m<sup>2</sup>/g). In order to confirm the location of TiO<sub>2</sub> clusters inside the channels of the SBA-15 substrate, the normalized  $S_{\text{BET}}$  ( $NS_{\text{BET}}$ ) was calculated according to Ref. [44]. For all hybrid  $x\%$  TiO<sub>2</sub>/SBA-15 materials, the  $NS_{\text{BET}}$  values fall in the range 0.62–0.76 (Table 1) suggesting some blocking of the SBA-15 pores with the guest TiO<sub>2</sub> particles located inside them. As expected, the 31% TiO<sub>2</sub>/SBA-15 material possesses a largest amount of the TiO<sub>2</sub> clusters located within the inner structure of SBA-15, as deduced from its lowest  $NS_{\text{BET}}$  value.

### 3.2. Structural characteristics

#### 3.2.1. Small-angle X-ray diffraction (XRD)

The hexagonal arrangement of the SBA-15-supported titania catalysts was confirmed from the low-angle XRD patterns (Fig. 3). The peak at ca. 1.8° is due to the diffraction plane [1 0 0], which indicates hexagonal symmetry. The transmission electron micrograph (TEM) images further verified the results of the low-angle XRD patterns. As example, Fig. 4 shows the TEM images of the 22% TiO<sub>2</sub>/SBA-15 sample. A well-ordered hexagonal array of mesopores can be seen when the electron beam is parallel to the main axis of the cylindrical pores. When the electron beam is perpendicular to

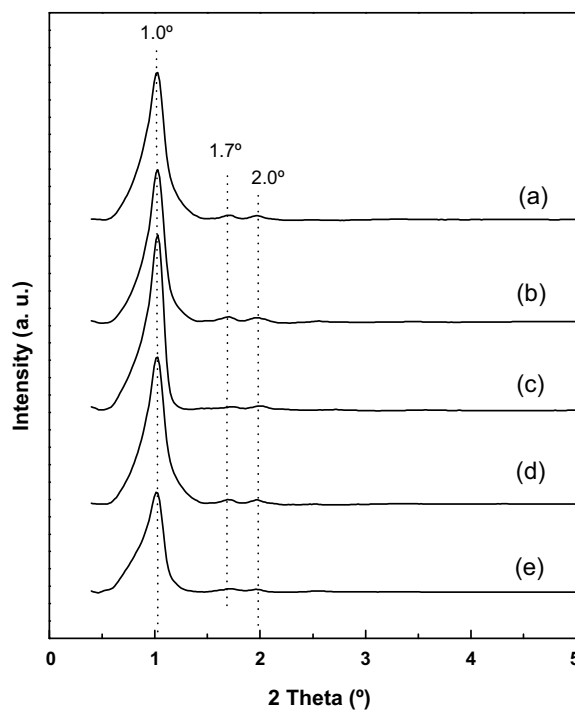


**Fig. 3.** Small-angle XRD patterns of  $x\%$  TiO<sub>2</sub>/SBA-15 and SBA-15 mesoporous samples: (a), naked SBA-15; (b), 12% TiO<sub>2</sub>; (c), 22% TiO<sub>2</sub>; (d), 26% TiO<sub>2</sub>; and (e), 31% TiO<sub>2</sub>.

the main axis, the presence of the parallel nanotubular pores of the parent SBA-15 matrix is evidenced. Similarly, for the other Ti-containing catalysts having a larger Ti content the introduction of TiO<sub>2</sub> does not alter the regular ordered array of mesopores.

#### 3.2.2. Wide-angle X-ray diffraction (XRD)

Wide-angle XRD patterns were recorded with the aim to investigate the presence of any crystalline species in the mesoporous  $x\%$  TiO<sub>2</sub>/SBA-15 matrices (Fig. 5). As can be seen in Fig. 5, all mesoporous matrices reveal diffraction patterns with a very broad peak at around  $2\theta = 24^\circ$  corresponding to amorphous silica [45]. The XRD patterns of the samples with 26 and 31 wt.% of TiO<sub>2</sub> evidence that anatase is the only titania phase present in these systems, as indicated by the peaks at  $2\theta = 24.5^\circ, 38^\circ, 48^\circ, 54.5^\circ, 62.5^\circ, 70^\circ$  and  $75^\circ$  (JCPDS-ICDD 21-1272). For the 26% TiO<sub>2</sub>/SBA-15 and 31% TiO<sub>2</sub>/SBA-15 samples, the titania crystal sizes calculated following the Scherrer equation were 13.5 and 12.6 nm, respectively. For the photocatalysts with a lower TiO<sub>2</sub> content than 26 wt.%, the absence of the peaks suggests the presence of well dispersed crystals of anatase phase or that species are amorphous. For all  $x\%$  TiO<sub>2</sub>/SBA-15 catalysts, no peak of (1 1 0) rutile reflection at  $27.4^\circ$  was detected.

#### 3.2.3. Infrared spectroscopy

FT-IR spectra of the samples calcined at 550 °C for 5 h are shown in Fig. 6. In all spectra, the peaks at around 3430 (not shown here) and 1633 cm<sup>-1</sup> are due to the stretching vibration of hydroxyl groups in surface-adsorbed water and Si–OH or Ti–OH of the mesoporous materials, respectively [46]. In the 1400–400 cm<sup>-1</sup> region of framework vibration, the vibration band at ca. 1085 cm<sup>-1</sup> corresponds to the asymmetric stretching vibration of Si–O–Si, and the peaks at 800 and 460 cm<sup>-1</sup> can be assigned to the symmetric stretching and deformation modes of Si–O–Si [47], respectively. As shown in Fig. 6, a weak peak at about 960 cm<sup>-1</sup> is observed for all samples. Theoretically, the IR bands observed at 910–960 cm<sup>-1</sup> can be assigned to the Si–O–Ti and Si–O–Si stretching vibration [46]. Upon addition of TiO<sub>2</sub>, a small shift of about 6 cm<sup>-1</sup> to lower



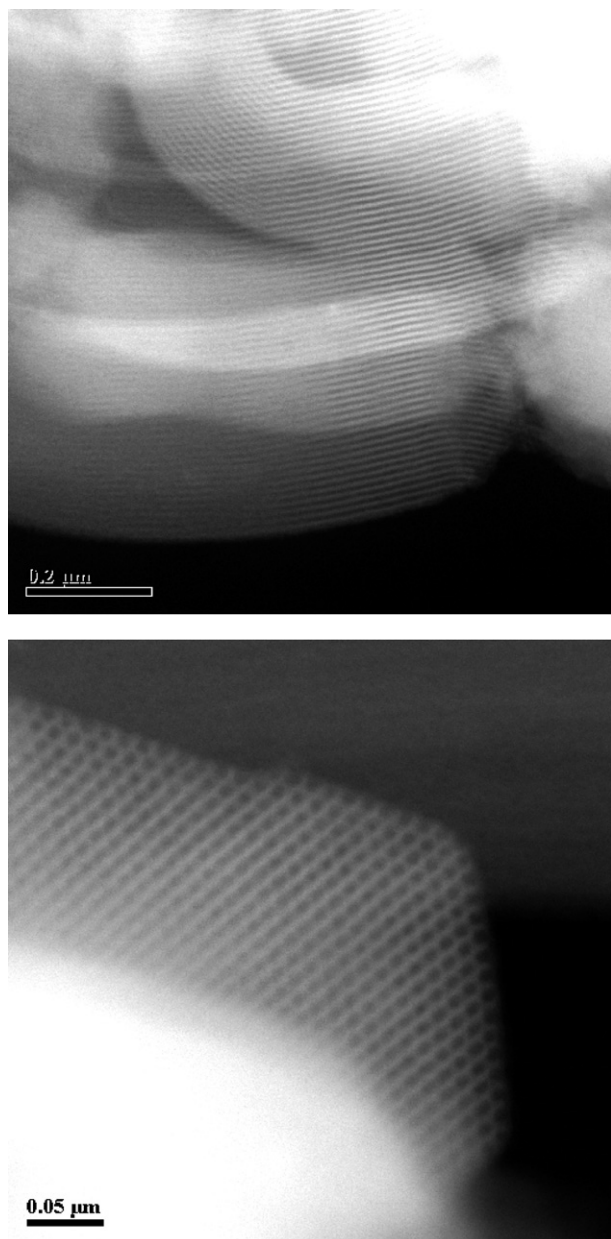


Fig. 4. TEM images of 22%TiO<sub>2</sub>/SBA-15 material showing parallel nanotubular pores (top) and well-ordered hexagonal array of mesopores (bottom).

frequencies is observed. These results provide strong evidence that the incorporated TiO<sub>2</sub> particles have been structurally combined with SiO<sub>2</sub> particles, resulting in the formation of TiO<sub>2</sub>–SiO<sub>2</sub> mixed oxides in all samples. Besides, a broad absorption in the range 400–800 cm<sup>−1</sup> grows with Ti content. This feature is evidence of TiO<sub>2</sub> as a separate phase (samples with 26 and 31 wt.% of TiO<sub>2</sub>).

### 3.2.4. Micro-Raman spectroscopy

As generally known, only the anatase crystal phase of titania shows good photocatalytic behavior as well as mixtures of anatase with small amounts of rutile or brookite. Therefore, the crystal phase of the *x*% TiO<sub>2</sub>/SBA-15 photocatalysts was determined with micro-Raman spectroscopy. Fig. 7 illustrates samples with 26 and 31 wt.% of TiO<sub>2</sub> and pure TiO<sub>2</sub>, each having four modes at 640, 520, 400, and 150 cm<sup>−1</sup> with an additional shoulder at 200 cm<sup>−1</sup>. Peaks at 640, 200, and 150 cm<sup>−1</sup> may be due to *E<sub>g</sub>* symmetric modes, and the peak at 520 cm<sup>−1</sup> is due to two modes of *B<sub>1g</sub>* and *A<sub>1g</sub>* symmetry

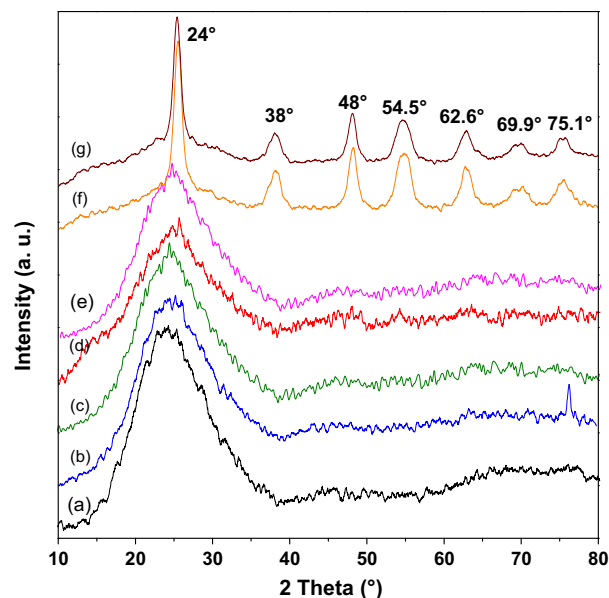


Fig. 5. Wide-angle XRD patterns of *x*%TiO<sub>2</sub>/SBA-15 mesoporous samples: (a), naked SBA-15; (b), 7% TiO<sub>2</sub>; (c), 12% TiO<sub>2</sub>; (d), 18% TiO<sub>2</sub>; (e), 22% TiO<sub>2</sub>; (f), 26% TiO<sub>2</sub>; and (g), 31% TiO<sub>2</sub>.

[48,49]. The Raman spectra indicate clearly that only the anatase phase of TiO<sub>2</sub> exists in these materials. For the mesoporous systems with the TiO<sub>2</sub> loading lower than 22 wt.%, the intensity all bands are very low indicating that the size of TiO<sub>2</sub> particles are very small, which is consistent with powder XRD and FT-IR. These patterns suggest that the rutile phase was not formed, confirming the enhanced thermal stability of TiO<sub>2</sub> by the introduction of a restricting SiO<sub>2</sub> phase. Anderson and Bard [50] suggested that the ability of the surrounding SiO<sub>2</sub> lattice to lock the Ti–O species with the SiO<sub>2</sub> at the interface prevents the diffusion and nucleation that is necessary for the phase transformation of the anatase to the rutile form.

### 3.2.5. UV–vis diffuse reflectance spectra (DRS)

Fig. 8 shows the UV–vis absorption spectra of calcined TiO<sub>2</sub>/SBA-15 and nanosized titania. There is a blue shift of the ultra-violet light absorption edge TiO<sub>2</sub>/SBA-15 compared with the nanosized anatase pure TiO<sub>2</sub>. The blue shift is introduced by the quantum effect of the semiconductor compound. TiO<sub>2</sub> is a large band gap semiconductor and the blue shift is attributed to the well

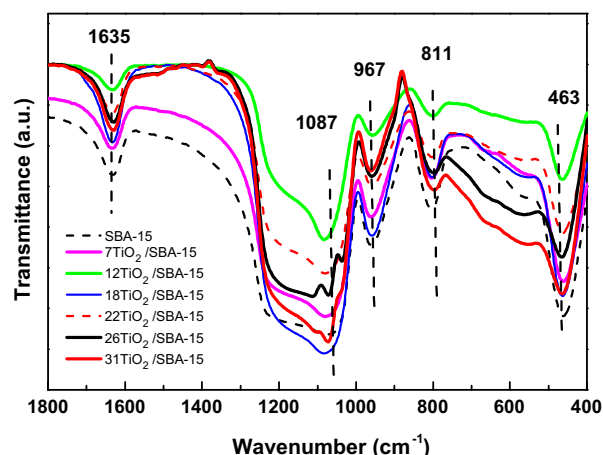


Fig. 6. FT-IR-KBr spectra of *x*%TiO<sub>2</sub>/SBA-15 samples.

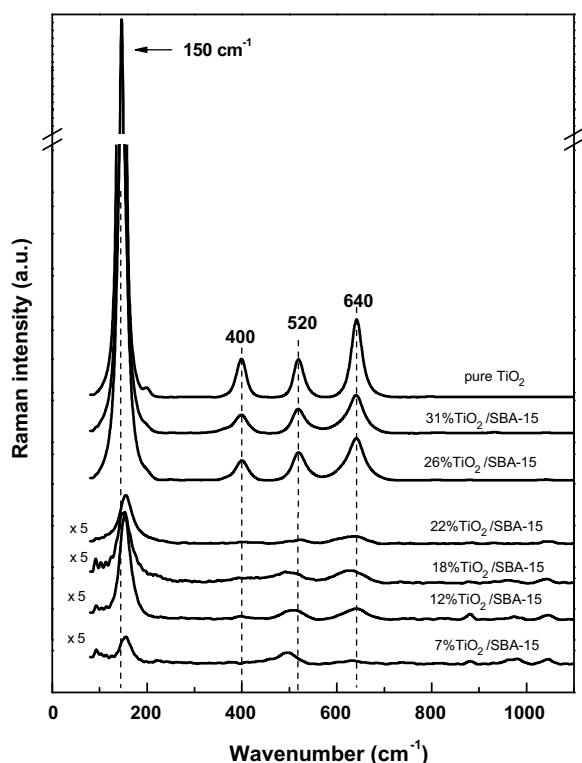


Fig. 7. Micro-Raman spectra of  $x\%$   $\text{TiO}_2/\text{SBA-15}$  and pure  $\text{TiO}_2$  samples.

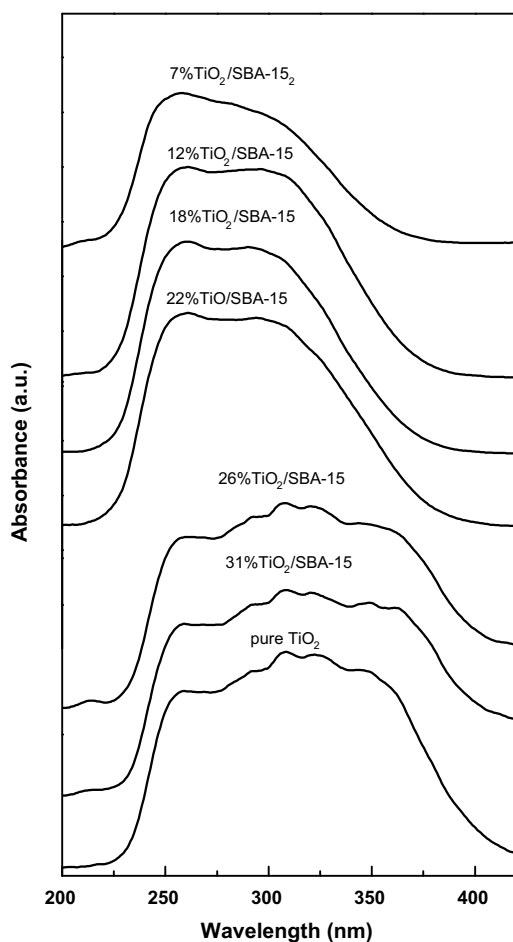


Fig. 8. DRS UV-vis spectra of  $x\%$   $\text{TiO}_2/\text{SBA-15}$  and pure  $\text{TiO}_2$  samples.

known quantum size effect for semiconductors as the particle size decreases [45,51]. The blue shift of the adsorption edge indicates the increase in the forbidden band energy, so the blue shift of the absorption edge of the UV-vis scattering pattern shows the smaller  $\text{TiO}_2$  particle size. In addition, the UV-vis scattering pattern indicates the coordination condition of the  $\text{Ti}^{4+}$  in the  $\text{TiO}_2$ . In fact the forbidden band adsorption edge site of  $\text{TiO}_2$  in UV-vis scattering pattern is related to the electron migration between  $\text{Ti}^{4+}$  and O. The forbidden band adsorption edge site is mainly decided by the coordination of Ti and the  $\text{TiO}_2$  grain size. When the  $\text{Ti}^{4+}$  ions coordination in the  $\text{TiO}_2$  aggregates increases, the adsorption edge will shift to higher wavelength. Furthermore, the broaden adsorption peak at about 230 nm in Fig. 8 is caused by the electron migration between the tetrahedral site of  $\text{Ti}^{4+}$  and O. This is because the hydrophilic nature of the silica surface, which favors the presence of hydrated titanium in tetrahedral coordination (230 nm), as already seen for amorphous silica-supported titanium catalysts [52]. The strong adsorption peak at about 280–300 nm was led by the titanium atoms in octahedral coordination [52] which are well-distributed and the particle size is smaller than 5 nm. When the adsorption wavelength is between 350 and 400 nm, it is caused by the  $\text{TiO}_2$ , which is bigger than 5 nm. The behavior of the UV-vis spectra shows the same curve shape as well as band edge for all calcined samples. Finally, in good agreement with XRD data, both 26%  $\text{TiO}_2/\text{SBA-15}$  and 31%  $\text{TiO}_2/\text{SBA-15}$  catalysts show a broad band at 370–410 nm confirming the presence of free  $\text{TiO}_2$  in those catalysts [52].

### 3.2.6. X-ray photoelectron spectroscopy (XPS)

The XPS technique has been used to examine the chemical state of the elements of the photocatalysts calcined at 550 °C. The binding energies of core electrons and Ti/Si surface atomic ratios of the naked SBA-15 and  $x\%$   $\text{TiO}_2/\text{SBA-15}$  catalysts are compiled in Table 2. O 1s core level spectra of the  $x\%$   $\text{TiO}_2/\text{SBA-15}$  samples are presented in Fig. 9. As expected, the pure SBA-15 shows only the bond at 532.8 eV assigned to oxygen in Si–O–Si (Table 2). On the contrary to this sample, two O 1s core level peaks at  $532.8 \pm 0.1$  eV and 530.0–530.6 eV are observed for  $x\%$   $\text{TiO}_2/\text{SBA-15}$  samples, which are assigned to oxygen in Si–O–Si and Ti–O–Ti in free  $\text{TiO}_2$  phase, respectively [53]. As expected, the increase of  $\text{TiO}_2$  loading of the  $x\%$   $\text{TiO}_2/\text{SBA-15}$  samples results in a continuous increase in intensity of the 530.0–530.6 eV peak suggesting a larger presence of separate  $\text{TiO}_2$  phases on the catalyst surface, in good agreement with XRD and UV-vis data. The BE at 530.2 eV (Ti–O–Ti) was observed for Ti-SBA-15 materials with bulk anatase  $\text{TiO}_2$  dispersed on the surface of the SBA-15 [54]. Finally, for the Ti  $2p_{3/2}$  core level, the BE values in range 458.7–459.3 eV are indicative of octahedrally coordinated  $\text{TiO}_2$  species [39]. It is therefore believed that the titanium species present on the external surface of  $x\%$   $\text{TiO}_2/\text{SBA-15}$  catalysts are constituted of isolated  $\text{TiO}_2$  clusters decorating surface of SBA-15.

The surface exposure of  $\text{TiO}_2$  species is visualized in Fig. 10(a). As expected, the surface exposure of  $\text{TiO}_2$  species increases with an increase in the  $\text{TiO}_2$  loading of catalysts. The exception is the 31%  $\text{TiO}_2/\text{SBA-15}$  sample, which exhibits a lower surface exposure of Ti-species than its 26%  $\text{TiO}_2/\text{SBA-15}$  counterpart. Considering the normalized specific surface area of both catalysts (Table 1), the former sample possesses a larger quantity of  $\text{TiO}_2$  species located within the SBA-15 pore network. This was confirmed by presenting the surface Ti/Si atomic ratio (from XPS) of the photocatalysts as function of their bulk Ti/Si atomic ratio (calculated from ICP-AES analysis) (Fig. 10(b)). The solid line in Fig. 10(b) shows the expected values for a homogeneous Ti distribution within the solid. It is seen that photocatalysts with  $\text{TiO}_2$  loading larger than 12 wt.% possess  $\text{TiO}_2$  species located mainly on the external catalyst surface. It is noteworthy that 31%  $\text{TiO}_2/\text{SBA-15}$  sample shows a more

**Table 2**Binding energies (eV) of core electrons and surface atomic ratios of the mesoporous TiO<sub>2</sub>-SBA 15 materials.

Catalyst	Si 2p	Ti 2p <sub>3/2</sub>	O 1s	Ti/Si at XPS	Ti/Si at bulk
SBA-15	103.4	–	532.8		
7% TiO <sub>2</sub> /SBA-15	103.4	459.3	530.6 (6) 532.9 (94)	0.060	0.060
12% TiO <sub>2</sub> /SBA-15	103.4	459.0	530.5 (26) 532.9 (74)	0.112	0.102
18% TiO <sub>2</sub> /SBA-15	103.4	458.7	530.3 (37) 532.8 (63)	0.427	0.160
22% TiO <sub>2</sub> /SBA-15	103.4	458.7	530.1 (44) 532.7 (56)	0.530	0.211
26% TiO <sub>2</sub> /SBA-15	103.4	458.7	530.0 (51) 532.8 (49)	0.690	0.266
31% TiO <sub>2</sub> /SBA-15	103.4	458.8	530.3 (47) 532.8 (53)	0.616	0.339

homogeneous distribution of the TiO<sub>2</sub> clusters than its 26% TiO<sub>2</sub>/SBA-15 counterpart. Both catalysts with the lowest TiO<sub>2</sub> loading (7 and 12 wt.%) are unique showing homogeneous TiO<sub>2</sub> distribution.

### 3.3. Photocatalytic activity

The photocatalytic activity of the x% TiO<sub>2</sub>/SBA-15 samples was evaluated in the degradation of methylene blue (MB). The objective was to compare their catalytic response with that of a commercial anatase TiO<sub>2</sub> (P-25, Degussa), which is the standard system employed in the field of photocatalytic reactions. This reference material contains anatase and rutile phases in a ratio of about 3:1 and it shows specific area of 49.2 m<sup>2</sup>/g [55]. The reaction

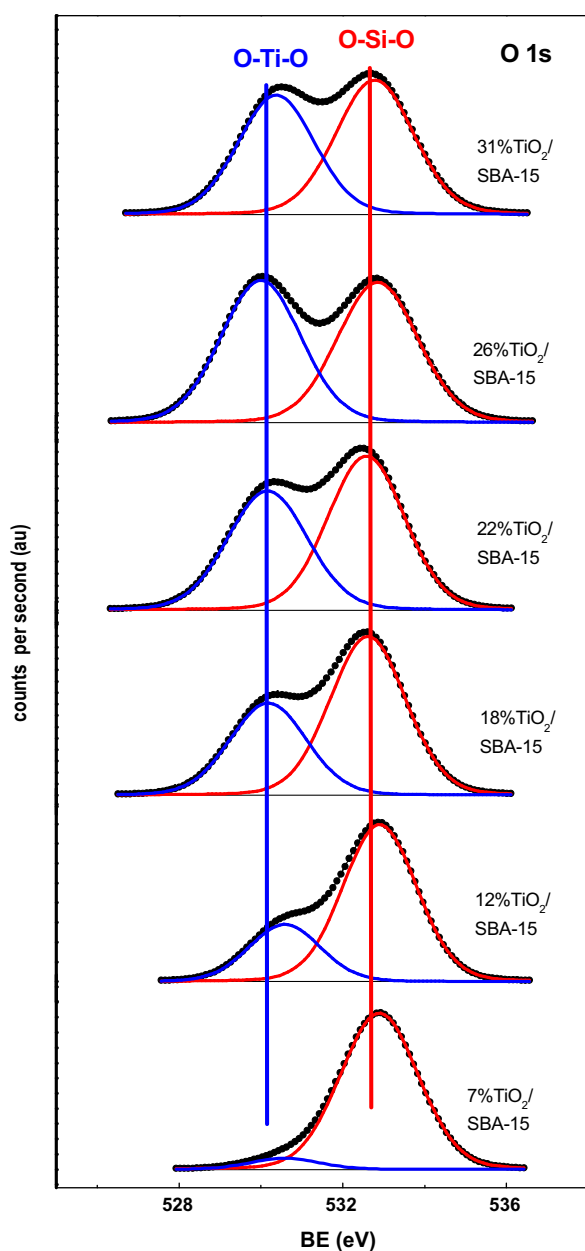


Fig. 9. O 1s core-level spectra of x% TiO<sub>2</sub>/SBA-15 mesoporous samples.

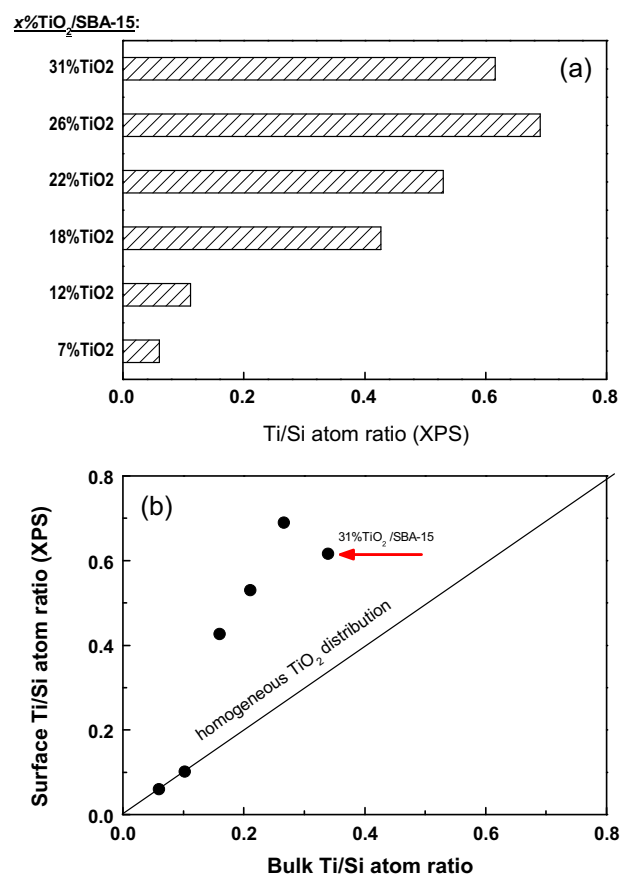
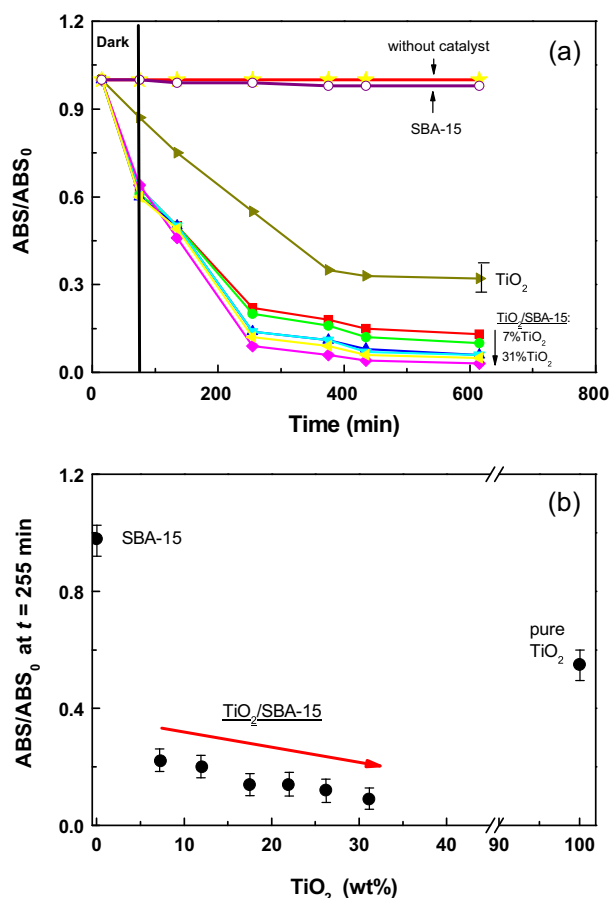


Fig. 10. (a) Comparison of Ti/Si atomic ratio of x% TiO<sub>2</sub>/SBA-15 samples. (b) Surface Ti/Si atomic ratio (from XPS) versus bulk Ti/Si atomic ratio (from ICP-AES). Solid line shows the expected values for a homogeneous Ti distribution within the solid.



**Fig. 11.** (a) Photocatalytic decomposition of methyl blue on  $x\%$   $TiO_2$ /SBA-15 samples and pure  $TiO_2$ . (b) Single point adsorption measurements at irradiation time of 255 min.

mechanism of MB degradation over heterogeneous  $TiO_2$  catalyst is based on Langmuir–Hinshelwood–Hougen–Watson (LHHW) mechanism and consisted of adsorption, surface reaction and desorption [56]. In other words, in photodegradation experiments there are two factors resulting in the decrease of MB concentration: the adsorption of the MB onto the photocatalyst's surface and the photodegradation of MB.

The extent of the MB adsorption on the catalysts was evaluated in the dark. Fig. 11(a) shows the change in the degradation curves of MB in 75 min. Blank experiments were also carried out in the absence of a catalyst and in the presence of SBA-15. No obvious photodegradation was observed in either case. Using  $x\%$   $TiO_2$ /SBA-15 without UV irradiation along the first hour, the concentration of MB rapidly decreased and discolored 40% of MB, which is due to the adsorption of MB on the catalyst's surface. In the absence of irradiation, the  $x\%$   $TiO_2$ /SBA-15 samples exhibit a much higher adsorption capability of the MB than pure titania. Considering the textural properties of the hybrid systems (Table 1), the superior activity of the hybrid materials is due to their much higher specific area (659–395 versus 49.2  $m^2/g$ ) and pore volume. Considering that typically experimental error, the adsorption of MB in the dark is more or less the same for all  $x\%$   $TiO_2$ /SBA-15 samples. This result indicates that the photocatalytic activity of the hybrid  $x\%$   $TiO_2$ /SBA-15 samples does not depend on the adsorption ability of composite being the photocatalytic activity of titania the main factor influencing on the catalyst activity, in line with the study by Yang et al. [57].

Considering the changes in the degradation curves of MB during irradiation (Fig. 11(a)), one might note that all  $x\%$   $TiO_2$ /SBA-15

**Table 3**

Apparent first-order rate constants ( $k_{app}$ ) of methylene blue degradation over  $TiO_2$ /SBA-15 and  $TiO_2$  materials.

Catalyst	Rate constant ( $min^{-1}$ )
7% $TiO_2$ /SBA15	0.0068
12% $TiO_2$ /SBA15	0.0076
18% $TiO_2$ /SBA15	0.0106
22% $TiO_2$ /SBA15	0.0106
26% $TiO_2$ /SBA15	0.0117
31% $TiO_2$ /SBA15	0.0136
Pure $TiO_2$	0.0026

samples showed more stable absorbance after irradiation time of 255 min. This is probably due to the competitive co-adsorption of MB and recalcitrant by-products that absorb at the same wavelength as MB. Unfortunately, considering the limitation of UV–vis equipment employed, it was not possible to evaluate the extent of mineralization of MB leading to formation of harmless gaseous  $CO_2$ ,  $NH_4^+$  and  $NO_3^-$  species. Fig. 11(b) shows single point adsorption data at irradiation time of 255 min as a function of the  $TiO_2$  content of the  $x\%$   $TiO_2$ /SBA-15 systems. It can be seen that the photocatalytic activity obeys the following order:  $x\%$   $TiO_2$ /SBA-15 > pure  $TiO_2$  > SBA-15 (none). Thus, it can be seen that the addition of  $TiO_2$  to SBA-15 substrate significantly improves the photodegradation activity of the catalysts, in good agreement with previous studies [58]. However, considering the experimental error (typically about 5% of  $ABS/ABS_0$ ), the adsorption of MB at irradiation time of 255 min is more or less the same for all  $x\%$   $TiO_2$ /SBA-15 samples.

It is well established that the kinetics of photocatalytic degradation of methylene blue obeys a first order kinetics model [59,60]. The reaction can be represented as follows (Eq. (1)):

$$R = -\frac{dC}{dt} = \frac{k_r KC}{1 + KC} \quad (1)$$

where  $k_r$  is the reaction rate constant,  $K$  is the adsorption coefficient of the methylene blue at the surface of  $x\%$   $TiO_2$ /SBA-15 samples and  $C$  is the concentration of the MB solution. When concentration of the MB in solution ( $C$ ) is very small, the  $KC$  value is negligible with respect to unity so that Eq. (1) describes first-order kinetics. The integration of this equation with the limit condition that at the start of irradiation ( $t = 0$ ), the concentration is the initial one,  $C = C_0$ , given in Eq. (2):

$$-\ln\left(\frac{C}{C_0}\right) = k_{app}t = k_r Kt \quad (2)$$

where  $k_{app}$  is the apparent first-order reaction constant and  $C_0$  is initial concentration of the MB solution.

The values of apparent first-order reaction rate constants for  $x\%$   $TiO_2$ /SBA-15 are calculated and listed in Table 3. Since an important extent of substrate was removed during 600 min of whole experiment, only data from first 255 min of irradiation time were considered in the calculation of the kinetic data of methylene blue dye degradation. The comparison of the  $k_{app}$  values of the home-made samples with those reported in literature indicates that our results are similar to those reported by Sahu et al. [58]. As expected, it was found that the apparent reaction rate constant increased linearly with an increase of the  $TiO_2$  content of the catalysts (Fig. 12(a)). This is because the increase of  $TiO_2$  content led to an increase of the adsorption ability of catalyst. Besides this factor, other factors such as crystal phase, surface area, crystalline size and the localization of the  $TiO_2$  clusters, etc. also play an important role in 'catalysts' photo-activity. In this regard, a linear correlation between the apparent first order rate constants ( $k_{app}$ ) and the amount of  $TiO_2$  species located within inner porous structure of the SBA-15 substrate was found (Fig. 12(b)) confirming a good accessibility of MB molecules to the  $TiO_2$  active sites. This is why a stable mesoporous network of SBA-15 [61] might facilitate the diffusion of



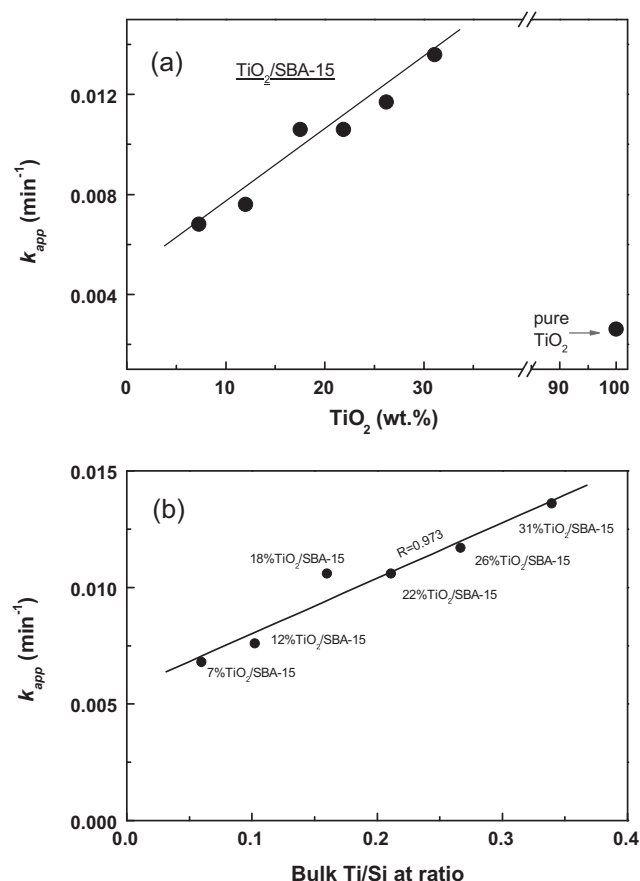


**Fig. 12.** (a) Apparent first order kinetic rate constants ( $k_{app}$ ) for the photodegradation of methylene blue on  $x\%$   $\text{TiO}_2/\text{SBA-15}$  samples against their  $\text{TiO}_2$  content. (b) Correlation between  $k_{app}$  and bulk Ti/Si atom ratio of those catalysts.

reactants and products, enhancing the activity by facilitating access to reactive sites of  $\text{TiO}_2$  [62].

The most active 31%  $\text{TiO}_2/\text{SBA-15}$  sample showed a more homogeneous  $\text{TiO}_2$  dispersion than its 26%  $\text{TiO}_2/\text{SBA-15}$  homologous, as deduced from the comparison of the surface and bulk Ti/Si atomic ratios of the catalysts (Fig. 10(b)). The  $\text{TiO}_2$  clusters of the former sample are a little smaller than on the later (12.6 versus 13.5 nm), as confirmed by XRD. The crystal size and homogeneous  $\text{TiO}_2$  dispersion are two important factors for the effective degradation because the organic material should be concentrated at the  $\text{TiO}_2$  surface firstly. Moreover, the large surface area of  $x\%$   $\text{TiO}_2/\text{SBA-15}$  samples also can adsorb significant amounts of water and hydroxyl groups, which could react with photo-excited holes on the catalyst's surface and produce hydroxyl radicals [63]. Moreover, taking into account that the surface acidity of  $\text{TiO}_2$  anatase is primarily Lewis in nature, one might expect that largest Lewis acidities of both catalysts with the largest  $\text{TiO}_2$  loading (26 and 31 wt.%) may contribute to their catalytic response [64]. Thus, the combined factors such as a larger porosity, higher specific area and acidity, and better accessibility of photo-oxidative sites might explain why the hybrid  $x\%$   $\text{TiO}_2/\text{SBA-15}$  exhibited a larger photocatalytic effect on the degradation of MB than pure anatase titania.

#### 4. Conclusions

The mesoporous matrices decorated by  $\text{TiO}_2$  have been successfully synthesized by the sol–gel method. The results of the activity test indicated that  $x\%$   $\text{TiO}_2/\text{SBA-15}$  mesoporous matrices prepared for this study had better photocatalytic activity performance than

pure  $\text{TiO}_2$ . The highest photocatalytic activity of 31%  $\text{TiO}_2/\text{SBA-15}$  can be attributed to three factors. Firstly, the sample has high anatase crystallinity which means few lattice defects and easy separation of photogenerated electrons and holes. Moreover, the phase transformation of anatase-to-rutile and the crystal growth of crystalline are suppressed. Secondly, the SBA-15 decorated by  $\text{TiO}_2$  preserved a high surface area even at high  $\text{TiO}_2$  content and possess a strong surface adsorption ability to dye molecules. Thus, the photogenerated radicals such as hydroxyl and superoxide radicals can easily react with MB molecules adsorbed on the catalyst surface. Thirdly, the SBA-15 decorated by  $\text{TiO}_2$  possesses more surface hydroxyl groups than the  $\text{TiO}_2$ . The surface hydroxyl groups can capture the photo-induced holes, produce active hydroxyl radicals and prevent electron–hole recombination at the same time. Consequently, the SBA-15 decorated by  $\text{TiO}_2$  showed a high photocatalytic activity, even superior to a commercial  $\text{TiO}_2$  (P-25).

#### Acknowledgments

The authors are greatly thankful to Dr. R. Zanella Specia (CCADET, UNAM) for  $S_{BET}$  studies; Dr. C.L. Peza-Ledesma (CFATA-UNAM) for her support in micro-Raman and IR studies; C.R. Flores Farías (CINVESTAV-QRO) for UV–vis studies and Dr. E. Rivera for XRD measurements. The authors also thank Professor J.L.G. Fierro (ICP-CSIC, Madrid, Spain) for XPS analysis. Financial support by the Community of Madrid (Spain) and European Union (Project S2009/ENE-1743) is gratefully acknowledged.

#### References

- [1] O. Hamdaouia, F. Saoud, M. Chiha, E. Naffrechoux, Chem. Eng. J. 143 (2008) 73–84.
- [2] R. Sivaraj, C. Namasivayam, K. Kadirvelu, Waste Manag. 21 (2001) 105–110.
- [3] E. Forgacs, T. Cserhati, G. Oros, Environ. Int. 30 (2004) 953–964.
- [4] I.A. Tan, A.L.W. Ahmad, B.H. Hameed, J. Hazard. Mater. 154 (2008) 337–346.
- [5] V.K. Gupta, A. Suhas, V.K. Imran, Saini, Ind. Eng. Chem. Res. 43 (2004) 1740–1747.
- [6] Z. Aksu, Process Biochem. 40 (2005) 997–1026.
- [7] A. Fujishima, K. Honda, Nature 238 (1972) 37–38.
- [8] B. Oregan, M. Grätzel, Nature 353 (1991) 737–740.
- [9] C.S. Turchi, D.F. Ollis, J. Catal. 122 (1990) 178–192.
- [10] D.F. Ollis, H. Al-Ekabi (Eds.), Photocatalytic Purification and Treatment of Water and Air, Elsevier, Amsterdam, 1993.
- [11] Z. Wang, W. Cai, X. Hong, X. Zhao, F. Xu, C. Cai, J. Appl. Catal. B: Environ. 57 (2005) 223–231.
- [12] D. Beydoun, R. Amal, G.K.-C. Low, S. McEvoy, J. Phys. Chem. B 104 (2000) 4387–4396.
- [13] H.Y. Zhu, J. Orthman, J.-Y. Li, J.-C. Zhao, G.J. Churchman, E.F. Vansant, Chem. Mater. 14 (2002) 5037–5044.
- [14] X. Zhang, F. Zhang, K.-Y. Chan, Appl. Catal. A: Gen. 284 (2005) 193–198.
- [15] W.Y. Jung, B. Ho Noh, S.H. Baek, G.D. Lee, S.S. Park, S.S. Hong, React. Kinet. Catal. Lett. 91 (2007) 223–231.
- [16] K. Tennakone, C.T.K. Tilakaratne, I.R.M. Kottegoda, J. Photochem. Photobiol. A 87 (1995) 177–179.
- [17] J.S. Kresge, M.E. Leonowicz, W.J. Roth, J.C. Beck, Nature 359 (1992) 710–712.
- [18] D. Zhao, J. Feng, Q. Huo, N. Melosh, G.H. Fredrickson, B.F. Chmelka, G.D. Stucky, Science 279 (1998) 548–552.
- [19] D. Zhao, Q. Huo, J. Feng, B.F. Chmelka, G.D. Stucky, J. Am. Chem. Soc. 120 (1998) 6024–6036.
- [20] M.M. Mohamed, T.M. Salama, T. Yamaguchi, Colloids Surf. A: Physicochem. Eng. Asp. 207 (2002) 25–32.
- [21] A. Bhattacharyya, S. Kawi, M.B. Ray, Catal. Today 98 (2004) 431–439.
- [22] W. Wang, M. Song, Mater. Res. Bull. 41 (2006) 436–447.
- [23] S. Perathoner, P. Lanzafranco, R. Passalacqua, G. Centi, R. Schlögl, D.S. Su, Microporous Mesoporous Mater. 90 (2006) 347–361.
- [24] K. De Witte, P. Cool, I. De Witte, L. Ruys, J. Rao, G. Van Tendeloo, E.F. Vansant, J. Nanosci. Nanotechnol. 7 (2007) 2115–2511.
- [25] M.M. Mohamed, T.M. Salama, T. Yamaguchi, Colloids Surf. A 207 (2002) 25–32.
- [26] Y. Chen, Y. Huang, J. Xiu, X. Han, X. Bao, Appl. Catal. A: Gen. 273 (2004) 185–191.
- [27] A. Bhattacharyya, S. Kawi, M.B. Ray, Catal. Today 98 (2004) 431–439.
- [28] K. Moggyorósi, J. Németh, I. Dékány, J.H. Fendler, Prog. Colloid Polym. Sci. 117 (2001) 88–93.
- [29] K. Moggyorósi, A. Farkas, I. Dékány, I. Ilisz, A. Dombi, Environ. Sci. Technol. 36 (2002) 3618–3624.
- [30] K. Moggyorósi, I. Dékány, J.H. Fendler, Langmuir 19 (2003) 2938–2946.
- [31] L. Liu, P. Dong, R. Liu, Q. Zhou, X. Wang, G. Yi, B. Cheng, J. Colloid Interface Sci. 288 (2005) 1–5.

- [32] H.-H. Choi, J. Park, R.K. Singh, *Appl. Surf. Sci.* 240 (2005) 7–12.
- [33] R. Van Grieken, J. Aguado, M.J. López-Muñoz, J. Marugán, J. Photochem. Photochem. A 148 (2002) 315–322.
- [34] M.V. Landau, L. Vradman, X. Wang, L. Titelman, *Microporous Mesoporous Mater.* 78 (2005) 117–129.
- [35] W. Wang, M. Song, *Microporous Mesoporous Mater.* 96 (2006) 255–261.
- [36] K. De Witte, P. Cool, I. De Witte, J. Rao, G. Van Tendeloo, E.F. Vansant, *J. Nanosci. Nanotechnol.* 7 (2007) 1–5.
- [37] T. Maschmeyer, F. Rey, G. Sanker, J.M. Thomas, *Nature (Lond.)* 378 (1997) 159–162.
- [38] K. Flodström, V. Alfredsson, *Microporous Mesoporous Mater.* 59 (2003) 167–176.
- [39] C.L. Peza-Ledesma, L. Escamilla-Perea, R. Nava, B. Pawelec, J.L.G. Fierro, *Appl. Catal. A: Gen.* 375 (2010) 37–48.
- [40] C.D. Wagner, W.M. Riggs, L.E. Davis, J.F. Moulder, G.E. Muilenberg, *Handbook of X-ray Photoelectron Spectroscopy*, Perkin Elmer Corp., 1979.
- [41] D. Zhao, Q. Huo, J. Feng, B.F. Chimelka, G.D. Stucky, *J. Am. Chem. Soc.* 120 (1998) 6024–6036.
- [42] P. Van Deer Voort, M. Benjelloun, E.F. Vansant, *J. Phys. Chem. B* 10 (2002) 9027–9032.
- [43] T.W. Kim, R. Ryoo, M. Kruk, K.P. Gierszal, M. Jaroniec, S. Kamiya, O. Terasaki, *J. Phys. Chem. B* 108 (2004) 11480–11489.
- [44] L. Escamilla-Perea, R. Nava, B. Pawelec, M.G. Rosmaninho, C.L. Peza-Ledesma, J.L.G. Fierro, *Appl. Catal. A: Gen.* 381 (2010) 42–53.
- [45] A. Tuel, L.G. Hubert-Pfalzgraf, *J. Catal.* 217 (2003) 343–353.
- [46] L.R. Oréfice, W.L. Vasconcelos, *J. Sol–Gel Sci. Technol.* 9 (1997) 239–249.
- [47] B. Pawelec, S. Damyanova, R. Mariscal, J.L.G. Fierro, I. Sobrados, J. Sanz, L. Petrov, *J. Catal.* 223 (2004) 86–97.
- [48] K. Parkodi, D.S. Arokiamary, *Mater. Charact.* 58 (2007) 495–503.
- [49] M. Li, Z. Feng, G. Xiong, P. Ying, Q. Xin, Ca. Li, *J. Phys. Chem. B* 105 (2001) 8107–8111.
- [50] C. Anderson, A.J. Bard, *J. Phys. Chem. B* 101 (1997) 2611–2616.
- [51] S. Klein, B.M. Werckhuysen, J.A. Martens, W.F. Maier, P.A. Jacobs, *J. Catal.* 163 (1996) 489–491.
- [52] M.C. Capel-Sanchez, J.M. Campos-Martin, J.L.G. Fierro, M.P. de Frutos, A. Padilla Polo, *Chem. Commun.* (2000) 855–856.
- [53] J. Feng, G. An, B. Chen, Y. Li, K. Ding, Y. Xie, Z. Lin, *Clean* 37 (2009) 527–533.
- [54] F. Bérubé, F. Kleitz, S. Kaliaguine, *J. Mater. Sci.* 44 (2009) 6727–6735.
- [55] H.E. Byrne, W.L.I.V. Kostedt, J.M. Stokke, D.W. Mazyck, *J. Non-Cryst. Solids* 355 (2009) 525–530.
- [56] A. Houas, H. Lachheb, M. Ksibi, E. Elaloui, C. Guillard, J.-M. Herrmann, *Appl. Catal. B* 31 (2001) 145–157.
- [57] J. Yang, J. Zhang, L. Zhu, S. Chen, Y. Zhang, Y. Tang, Y. Zhu, Y. Li, *J. Hazard. Mater. B* 137 (2006) 952.
- [58] D.R. Sahu, L.Y. Hong, S.-C. Wang, J.-L. Huang, *Microporous Mesoporous Mater.* 117 (2009) 640–649.
- [59] C.M. Ling, A. Rahman Mohamed, S. Bhatia, *AJChE* 5 (2) (2005) 131–139.
- [60] S.-Y. Kim, T.-H. Lim, T.-S. Chang, C.-H. Shin, *Catal. Lett.* 117 (3–4) (2007) 112–118.
- [61] M. Kruk, M. Jaroniec, C.H. Ko, *Chem. Mater.* 12 (2000) 1961–1968.
- [62] Z. Shan, E. Gianotti, J.C. Jansen, J.A. Peters, L. Marchese, T. Maschmeyer, *Chem. Eur. J.* 7 (2001) 1437–1443.
- [63] C.S. Turchi, D.F. Ollis, *J. Catal.* 22 (1990) 178–192.
- [64] J. Papp, S. Soled, K. Dwight, A. Wold, *Chem. Mater.* 6 (1994) 496–500.